doi:10.26443/seismica.v4i2.1675

Near Vent Seismicity at the Tour Eiffel Vent Site, Lucky Strike Hydrothermal Field, Mid-Atlantic Ridge

Soumya Bohidar * † [1], **Wayne C. Crawford** [1], **Mathilde Cannat** [1]

[1]Université Paris Cité, Institut de Physique du Globe de Paris, CNRS, 75005 Paris, France

Author contributions: *Conceptualization*: Crawford, Cannat. *Methodology*: Bohidar, Crawford. *Software*: Bohidar, Crawford. *Formal Analysis*: Bohidar, Crawford. *Writing - Original draft*: Bohidar, Crawford, Cannat. *Writing - Review & Editing*: Bohidar, Crawford, Cannat. *Supervision*: Crawford, Cannat. *Project administration*: Crawford, Cannat.

Abstract Secondary hydrothermal circulation is created by local entrainment of cold seawater into the shallow subseafloor by the intense discharge of high temperature fluids through focused vents at black smoker hydrothermal fields. To improve our understanding of secondary hydrothermal circulation, we tested a new instrumentation consisting of a small-scale (∼150 m aperture) four-hydrophone network connected to single datalogger, which could potentially record very small and shallow microearthquakes associated with near-seafloor upflow of hydrothermal fluids and mineral precipitation. We report on a one-year catalog of near-seafloor microearthquakes, recorded with this hydrophone network deployed around the Tour Eiffel black smoker vent site of the Lucky Strike hydrothermal field. We detect 740 shallow microearthquakes (depth between 0 and 300 m, local magnitude between -4.0 and -0.5) that may be generated by reaction-driven cracking due to anhydrite precipitation in the shallow subseafloor. The seismicity rate is low, and the events are not focused around the black smokers, suggesting that heating of entrained seawater and anhydrite precipitation is not prevalent near these vents. This hypothesis is supported by time-series analysis of diffuse fluid samples from the Tour Eiffel site, which show little to no chemical evidence for anhydrite precipitation.

Production Editor: Andrea Llenos
Handling Editor: Meng Wei
Copy & Layout Editor: Tara Nye

Received: April 7, 2025
Accepted: November 14, 2025
Published: December 9, 2025

1 Introduction

Hydrothermal circulations at mid-ocean ridges (MORs) transport magmatic heat (Lister, 1972; Lowell et al., 1995) and chemicals (Elderfield and Schultz, 1996) from the solid Earth to the ocean. There are two types of hydrothermal vents at mid-ocean ridges: focused outflows of high temperature fluids and diffuse lower-temperature emissions, usually surrounding the focused vents (Corliss et al., 1979). Focused high temperature vents result directly from km-scale fluid hydrothermal cells which entail downward percolation of seawater through highly porous and permeable near surface rocks, followed by progressive chemical exchange with the host rocks, and heat extraction from underlying magmatic sources at depth (Lister, 1974; Wilcock and Delaney, 1996). Intense discharge of high temperature fluids through focused vents, often at temperatures > 300°C, can entrain cold seawater into the shallow subseafloor near the hot vents, known as secondary or entrained circulation (Humphris et al., 1995). The cold seawater mixes with the primary hydrothermal fluids (Butterfield et al., 2004; Edmond et al., 1979; Wheeler et al., 2024), or is conductively heated (Cooper et al., 2000), both processes creating low temperature diffuse fluids. Diffuse vents extend over a larger and more scattered area and are estimated to carry 50–95% of the hydrothermal heat flux (Baker et al., 1993; Mittelstaedt et al., 2012; Ramondenc et al., 2006). They also host a unique chemosynthetic microbial and hydrothermal fauna (Corliss et al., 1979; Cuvelier et al., 2009; Juniper et al., 1995). Secondary circulation leads to mineral precipitation from the entrained seawater in the form of anhydrite (Bischoff and Seyfried, 1978), and from the cooling high temperature fluids, forming hydrothermal deposits. Understanding the secondary circulation and the shallow upflow domain is important to understand dynamics of benthic ecosystems, global oceanic heat budgets and the formation of rare minerals.

Our current understanding of near-seafloor secondary circulation and the shallow upflow domain of high temperature fluids comes mostly from a few short drill cores recovered at the Trans-Atlantic Geotraverse (TAG) hydrothermal field at the slow spreading Mid-Atlantic Ridge (Humphris et al., 1995, 2015), near vent fluid sampling and geological observations (Barreyre et al., 2014; Butterfield et al., 2004; Cooper et al., 2000; Wheeler et al., 2024), and analytic and numerical models (Guo et al., 2020; Lowell et al., 2003; Lowell and Yao, 2002). The geometry and subsurface extent of the secondary circulation system remain largely unconstrained because the geophysical sensor arrays in most of the subseafloor monitoring setups are designed to monitor the primary hydrothermal system, whereas resolving smaller secondary circulation requires high-frequency data from dense, small-aperture (∼200–300 m) sensor arrays. Using such a configuration with short-

*Corresponding author: soumyabohidar@ncpor.res.in
†Now at the National Center for Polar and Ocean Research, Headland Sada, Vasco-da-Gama, Goa, 403804, India

period Ocean Bottom Seismometers (OBS), Pontbriand and Sohn (2014) constrained this secondary system beneath the TAG sulfide mound by characterizing shallow microearthquakes and proposed that these events were triggered by reaction-driven cracking in response to anhydrite precipitation from heated seawater in the secondary circulation system.

The Lucky Strike hydrothermal field, located at the top of Lucky Strike volcano, Mid-Atlantic Ridge (Fouquet et al., 1995; Humphris et al., 2002; Langmuir et al., 1997; Ondréas et al., 2009; Escartin et al., 2015) extracts heat from an axial magma chamber (AMC) (Combier et al., 2015; Singh et al., 2006), and hosts several active high-temperature venting sites (Fig. 1a). A long-term volcano-scale OBS network (2007–2019 with yearly redeployment, Fig. 1a) identifies an evolving seismicity cluster above the AMC and to the north of the main hydrothermal field, which is interpreted as resulting from enhanced hydrothermal cooling, tectonic cracking, and possible small dike injections near the base of the main hydrothermal circulation (Bohidar et al., 2024; Crawford et al., 2013).

The Tour Eiffel (TE) hydrothermal site, located in the southeast part of the hydrothermal field (Fig. 1b), is one of the largest Lucky Strike vent sites, extending over approximately 24 m × 20 m and is dominated by a ∼15 m high sulfide edifice, bearing several high temperature vents and surrounded by diffuse flow areas. The total heat flux, including both discrete and diffuse venting, is estimated to be ∼20 (Mittelstaedt et al., 2012) to 50 MW (Wheeler et al., 2024) with Mittelstaedt et al. (2012) estimating that more than 95% of the heat comes from diffuse venting. Geological mapping and time-series of diffuse fluid temperature and chemistry indicate a complex shallow permeability structure below Tour Eiffel hydrothermal site and show that anhydrite precipitation from entrained seawater is low in this region (Wheeler et al., 2024). Other notable high-temperature vent sites in the eastern part of the Lucky Strike hydrothermal field include Montségur (area: ∼24 m × 16 m), and relatively smaller Sintra and Y3 sites (area: ∼7 m × 5 m each) located about 70 m South and 250–300 m N–NW of Tour Eiffel site respectively.

To precisely detect and locate very small (M < 0) microearthquakes associated with near-seafloor upflow of hydrothermal fluids and mineral precipitation in the presumed secondary circulation zone, we tested a new instrumentation consisting of multiple hydrophones connected by 100-meter-long cables to one datalogger (called the 'Hydroctopus'), developed for the European Multidisciplinary Seafloor and water column Observatory (EMSO)-Azores. Using the same datalogger allows us to create a network with very precise (sub-sample) relative travel times, irrespective of clock drift. The tested instrument consists of four hydrophones separated by ∼100 m. Ideally, the system would consist of more hydrophones over a larger area, but the present system serves as a low-cost proof of concept. We present one year of near-seafloor microearthquakes recorded in the vicinity of the Tour Eiffel vent site using the Hydroctopus. The Hydroctopus detected several types of events, including whale songs and earthquakes originating outside the network and/or at depths greater than the few hundred-meter scope of this study. We therefore developed criteria to select shallow microearthquakes within or near the network based on waveform characteristics, number of phases, and frequency spectra. Although the location of these shallow microearthquakes is not well constrained because of the limited number of instruments and weak constraints on the uppermost crustal velocity structure, we obtain a first order picture of shallow microearthquake locations in the vicinity of the Tour Eiffel vent site. We discuss their possible source mechanisms and their implications for secondary hydrothermal circulation around the Tour Eiffel vent site.

2 Method

2.1 Experimental Setup

The Hydroctopus network consists of four HiTech HTI-04 hydrophones connected by ∼100 m cables to a single datalogger on one of the EMSO-Azores sea monitoring nodes (SEAMON East) in the southeast corner of the volcano summit (Fig. 1b). The sampling frequency of the hydrophones is 250 Hz, and the effective high-frequency cut-off is ∼100 Hz. After each deployment, the data acquisition system was recovered and reset, but the hydrophones remained in place except H3 hydrophone (central hydrophone, Fig. 1b), which was only moved by a few decimeters. We report results from the Hydroctopus network for the first time, from the first two consecutive deployments, spanning 2016-09-10 to 2017-09-25 (380 days).

As part of the EMSO-Azores observatory, a network of four-component five ocean bottom seismometers (OBSs) has also been deployed surrounding the volcano summit since 2007 with yearly redeployments (Fig. 1a, instrument specifications for the OBS network can be found in Bohidar et al., 2024). During the Hydroctopus deployment, only one OBS (hereafter referred to as N-OBS) was operational, located approximately 3.5 km north of the Hydroctopus system (Fig. 1a). We also compare the earthquake waveform characteristics recorded by the Hydroctopus network with those observed by N-OBS.

2.2 Event Detection and Classification

We detected events using a standard short-term average/long-term average (STA/LTA) algorithm, adapting the parameters to small, short duration events (STA/LTA > 2.2 for window lengths of 0.2 and 10 s, respectively). Prior to STA/LTA detection, the waveforms were filtered in 5–50 HZ frequency range, as shallow events detected by Pontbriand and Sohn (2014) using a similar aperture scale OBS network were mostly seen in 15–30 Hz. Events detected on all four hydrophones were selected for further analysis.

We developed a protocol to classify the different types of events detected by the Hydroctopus network and to identify shallow near-surface events. First we automatically removed whale songs from the total set of detections identified by the STA/LTA algorithm. Whale songs

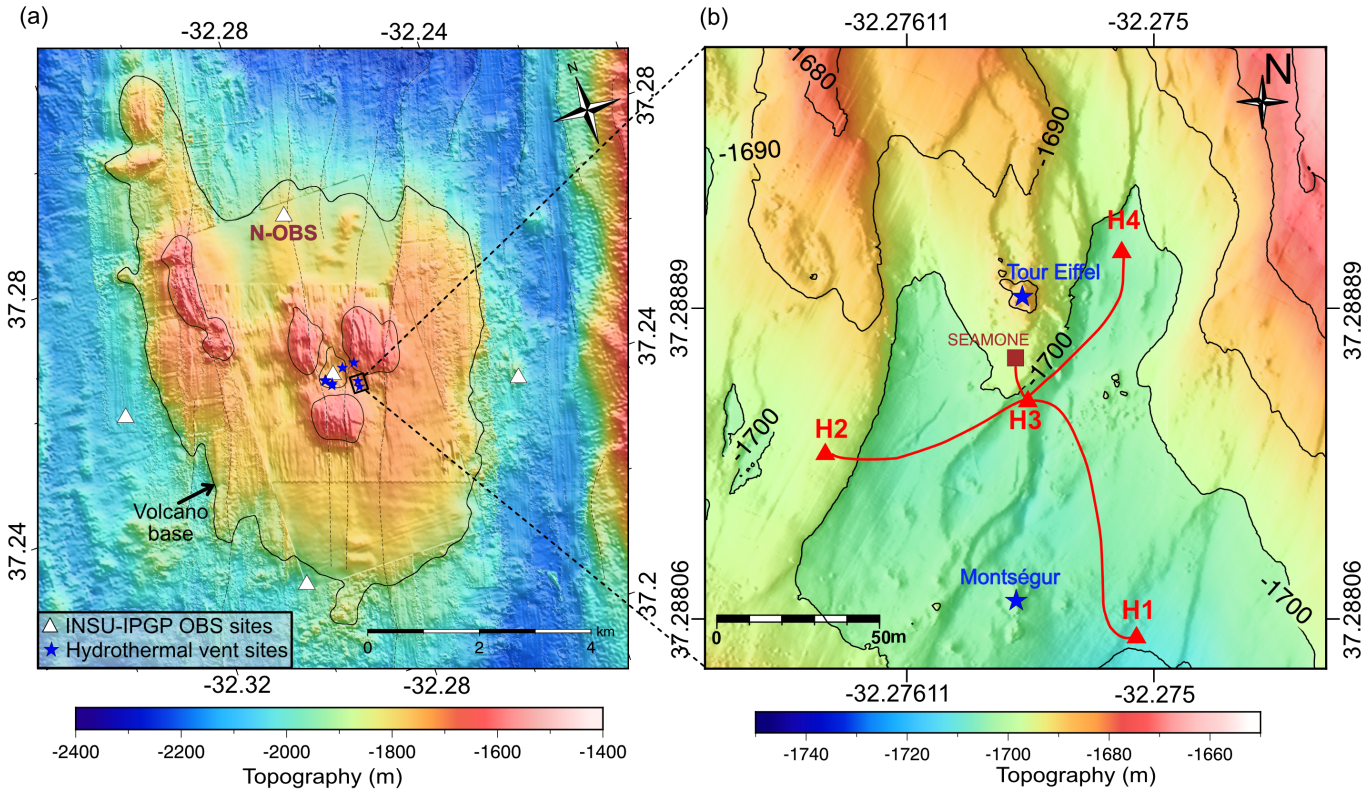

Figure 1 (a) Overview of Lucky Strike volcano, Mid-Atlantic Ridge. The solid black isocontours outline the volcano base (1900 m beneath seafloor) and its three peaks. Blue stars: Hydrothermal vent sites, White triangles: INSU IPGP OBS deployment sites (Only N-OBS data is used in this study as data from rest of the OBSs are unavailable/unusable during the Hydroctopus deployment). Black rectangle marks the Hydroctopus network region. (b) Overview map of the Hydroctopus array. Red triangles: hydrophones, Brown square: SEAMON-East (one of the Sea Monitoring nodes of the observatory), Blue stars: Hydrothermal vent sites, Black lines: Isocontours.

were distinguished based on the following characteristics: they typically consist of 2–3 s waveforms, with peak spectral energy concentrated between 20 and 30 Hz, and are repeated every 12–15 seconds, often continuing for several hours at a time (Fig. S1 in Supplementary Material). Subsequently, we applied an automatic classification method based on the number of detected phases, waveform duration, and dominant spectral frequency to categorize the remaining non-whale events. These classifications were then manually verified and corrected. The waveform duration was defined as total time interval of the seismic signal measured from the onset of first phase arrival to the end of the coda.

We focused the rest of the processing only on identified shallow near-surface events. We calculated relative P phase arrival times using phase cross-correlation. Taking the H3 hydrophone (center of the network, Fig. 1b) as our reference, we cross-correlated its waveform with the other hydrophone waveforms, calculating the offset as the time of the highest cross-correlation coefficient. For comparison with arrivals at other stations, we set the H3 hydrophone P phase arrival time to be the trigger time given by STA/LTA method.

Since hydrophones measure the pressure variations in the water column, they are generally unable to detect S phase (Shear waves). Therefore, no S phases were observed in the hydrophone data. Moreover, our analysis focused on very small-magnitude, shallow events; thus, even if any S phases were present, they would likely to have been obscured by noise.

2.3 Synthetic Waveform Modelling

To better constrain the different types of detected events, we performed synthetic waveform modelling of events with different source depths and receiver distances. We used the Fomosto (QSEIS backend; Heimann et al., 2019) tool within the Pyrocko library to calculate Green's functions, using a 1D velocity model (Fig. S2a and Text S1 in Supplementary Material) taken from a previous 3D P-wave velocity model (Arnulf et al., 2013), centered in the middle of Hydroctopus network. We used an explosive source (magnitude = -2.5) and calculated the amplitudes of the direct P and water reflected PwP phases for events in a depth range of 0–8 km beneath the seafloor and a horizontal distance range of 0–5 km, using the 250 Hz sampling frequency of the Hydroctopus.

2.4 Shallow Earthquake Location and Magnitude Estimation

We performed earthquake locations and magnitude estimation only on shallow near-surface events (Type-1 event, see Section 3.1 Event Classification). We estimated earthquake locations using a grid search algorithm within the NonLinLoc (NLLoc; Lomax et al., 2000) software, using a 1 km^3 cubic grid centered at site H3

hydrophone and with 10 m node spacing. Since the subseafloor shallow upper-crustal velocity structure is not well constrained, we tested various constant velocity gradient, shallow velocity models, with seafloor P-wave velocities ranging from 1.5 km/s to 3.2 km/s and gradients ranging from 0 to 3.6 (km/s)/km, selecting the model that yielded minimum root-mean-square (RMS) time error and minimum horizontal and vertical standard deviations for the event locations (Fig. S3 and Text S2 in Supplementary Material). The best-fitting model had a P-wave velocity of 1.5 km/s at the seafloor and a velocity gradient of 2.6 (km/s)/km, leading to a P-wave velocity of 4.1 km/s at the base of the model, 1 km beneath the seafloor.

Since this was a hydrophone network, we could not calculate the magnitude of the events directly from the signal. The primary network of OBSs did not have good quality data for the duration of the Hydroctopus deployment (except N-OBS) and shallow events detected by the Hydroctopus were only detected in the primary network OBS's hydrophone channels (discussed later). We therefore established an empirical relationship between the pressure amplitude on the hydrophone channel and the displacement amplitude on the vertical channel from the catalog of deeper on-volcano events recorded by the primary OBS network (Fig. S4 in Supplementary Material, 374 events recorded between April 2015 and May 2016; Bohidar et al., 2024). We verified that the OBS and Hydroctopus hydrophones had the same response using PPSD analysis (Fig. S5b in Supplementary Material), then converted the Hydroctopus hydrophone channel amplitudes to approximate displacements and calculated the local magnitudes using the custom scale defined in Crawford et al. (2013).

3 Results and Discussion

3.1 Event Classification

Based on the number of detected phases, waveform duration, and dominant spectral frequency, the non-whale events detected by the Hydroctopus network are classified into three main categories. Events that do not fit into these categories or whale calls are attributed to ship or other oceanic noise sources and are excluded from further analysis.

Type-1 events have very short durations (∼1 s) with only one detectable phase (direct P) on all four hydrophones (Fig. 2a-1 and Figs. S6–S7 in Supplementary Material). The maximum spectral energy is observed between 10–30 Hz (Fig. 2a-2). Type-1 events can present different waveform patterns and spectra on different hydrophones even though the hydrophones are very close to one another (Figs. S6–S7 in Supplementary Material). Type-2 events are ∼3 s and have two phases separated by ∼2.25–2.3 s (Fig. 2b-1), which we identify as direct P phase, and the water reflected P (PwP) phase from the sea-surface respectively (the two-way P-wave traveltime in the 1.7 km thick water column in this region is approximately 2.26 s assuming acoustic water velocity of 1.5 km/s). We further verified this by autocorrelating the event waveform with an inverted and 2.26 s delayed waveform. Type-2 P phase has the highest spectral energy between 15–30 Hz (Fig. 2b-2). Type-3 events are more than 15 s long, with direct P and PwP phases and a long coda after the PwP arrival (Fig. 2c-1). Type-3 P phase has the highest spectral energy between 8–10 Hz (Fig. 2c-2).

We looked for all three types of event waveform patterns in the vertical and hydrophone channels of the N-OBS, which was deployed ∼3.5 km north of the Hydroctopus (Fig. 1a). On the N-OBS, type-2 events show both direct P and S phases on the vertical channel, with an S–P traveltime difference of ∼0.8 s (Fig. 2b-4). On the N-OBS hydrophone channel, they have P and PwP phases separated by ∼2.3 s (Fig. 2b-3). Type-3 events show direct P and S phases with an S-P traveltime difference of ∼3.6 s on the vertical channel (Fig. 2c-4), and P and PwP phases with an PwP-P traveltime difference of ∼2.3 s on the hydrophone channel of the N-OBS (Fig. 2c-3). The average time differences between the first P phase in the Hydroctopus and the N-OBS for type-2 and type-3 events are ∼0.5 s and ∼1.1 s, respectively, indicating a clear bimodal distribution. Based on these observations and comparisons with the pre-existing seismicity catalog (Bohidar et al., 2024), we identify type-2 events as on-volcano deeper events (originated mainly above the 3-4 km deep melt lens; Bohidar et al., 2024), and type-3 events as segment-end/off-volcano events.

Type-1 events are very rarely seen on the N-OBS vertical channel, and only events with local magnitudes > -2.0 are seen on its hydrophone channel. On the N-OBS hydrophone channel, type-1 events are ∼1 s, with only direct P phase clearly detectable (Fig. 2a-3). The first P phase arrives 1.1 s to 1.8 s (average ∼1.54 s) later at N-OBS than on the Hydroctopus hydrophones for 70% of the events (Fig. 2a-3 and Fig. S8a in Suplementary Material). These delay times are consistent with very shallow events (< 300 m below seafloor) originating in the vicinity of the Hydroctopus. To verify this, we calculated the P travel time difference between the Hydroctopus hydrophone and the N-OBS hydrophone for synthetic events located 10 m horizontally from the center of the Hydroctopus network and from 0 to 1000 m beneath the seafloor (Fig. S8b in Supplementary Material). Delays between 1.1 and 1.8 seconds correspond to depths between 0 and 300 m, greater depths give smaller delays (0.6 s at 1000 m depth). We did not obtain delays greater than 1.8 s, probably because our simple synthetic model accounts neither for lateral velocity variations nor for complex depth structure.

We also calculated P to PwP phase amplitude ratios, using synthetic waveforms generated at different depths and distances from the Hydroctopus network. These ratios are in the range of 5 to 10 for events located within 200 m horizontally from the sensor and with source depths < 500 m (Fig. S2b in Supplementary Material). We believe that the PwP phase is generally not observed for type-1 events because the 5–10× smaller signal is generally below the background noise level.

Based on the above analyses, we consider type-1 events to be shallow (with 90% of events < 500 m beneath the seafloor) because of their short durations, apparent

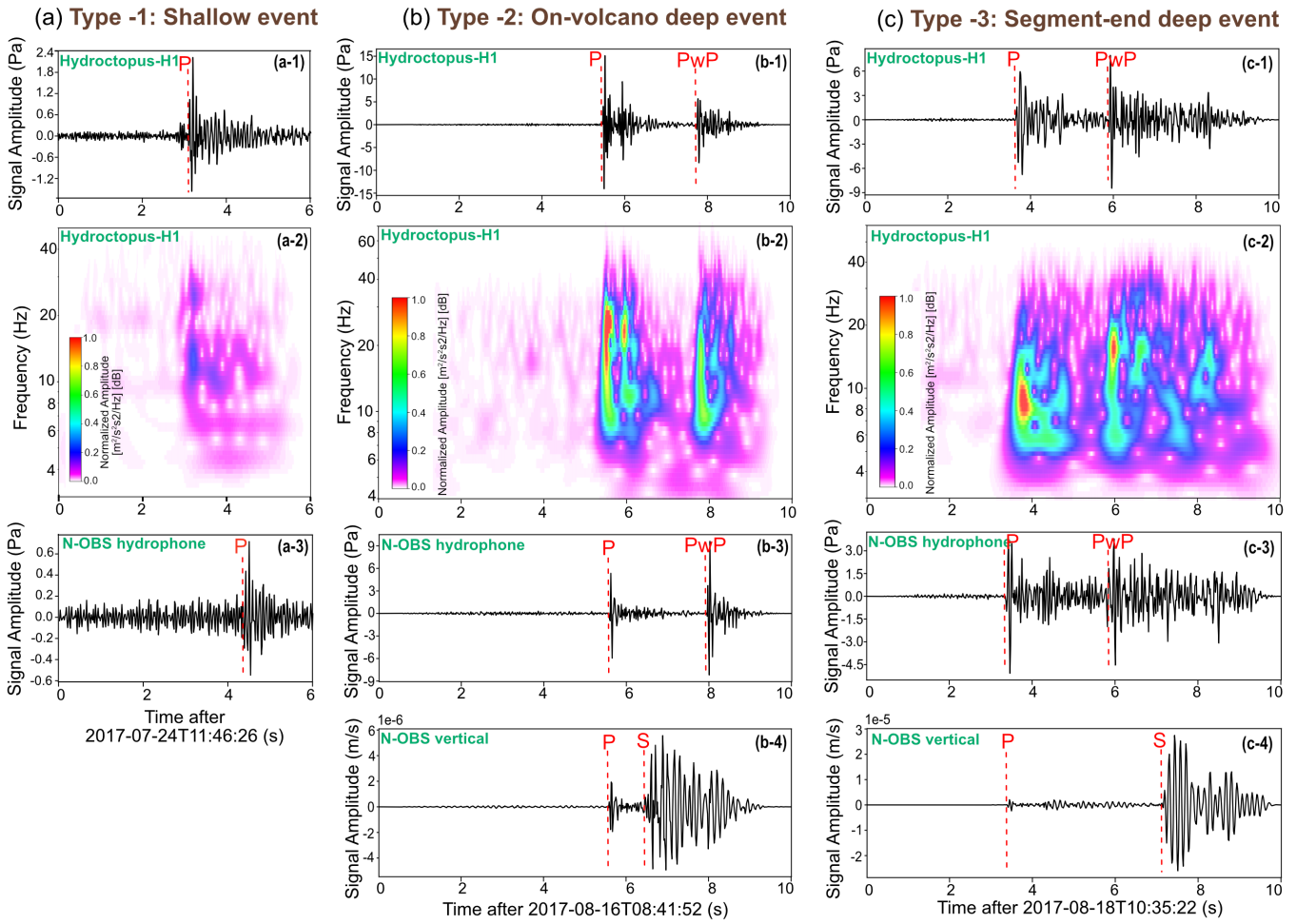

Figure 2 Examples of types of events detected by the Hydroctopus network. X-axis scale is same on each column, but Y-axis scale is different based on signal strength. (a) Example of a Type-1 (shallow) event. (a-1) & (a-2) are the shallow event waveform and respective frequency spectrum from H1 hydrophone of the Hydroctopus. (a-3) is the same event waveform from the N-OBS hydrophone channel. Waveform patterns for the rest of the Hydroctopus hydrophones are shown in Figs. S6–S7 in Supplementary Material. (b) Example of a Type-2 (On-volcano deep) event. (b-1) & (b-2) are the volcano deep event waveform and respective frequency spectrum from H1 hydrophone of the Hydroctopus. (b-3) & (b-4) are the same event waveforms from the N-OBS hydrophone channel & N-OBS vertical channel respectively. (c) Example of a Type-3 (segment-end deep) event. (c-1) & (c-2) are the segment-end deep event waveform and respective frequency spectrum from H1 hydrophone of the Hydroctopus. (c-3) & (c-4) are the same event waveforms from the N-OBS hydrophone channel & N-OBS vertical channel respectively. Red dashed lines mark the identified seismic phases on each channel.

lack of PwP and S phases, and the P arrival delay at the N-OBS.

We identified 740 shallow events, 1089 on-volcano deep events, and 988 segment-end events in the September 2016–September 2017 Hydroctopus record (Fig. S9 in Supplementary Material). Very few shallow events were detected between November 2016 and March 2017, when whale songs were abundant (Fig. 3b and Fig. S9 in Supplementary Material). A similar effect is observed, to a lesser extent, for deeper events (Bohidar et al., 2024). Note that the total number of type-2 (on-volcano deeper) and type-3 (segment-end) events detected by the Hydroctopus network may not represent the actual number of events occurring during the experiment period. The Hydroctopus array aperture is very small (∼150 m) and is not designed to detect deeper events. Moreover, the STA/LTA parameters are adapted to detect shallow events only, which might have excluded some deeper events.

3.2 Shallow Microearthquake Location and Magnitude Estimation

The 740 shallow (Type-1) events have local magnitudes (M_L) ranging from -4.0 to -0.5 (magnitude of completeness: -2.3, b-value: 0.87; Fig. 3a). Outside of the period when whale songs obscure the record, shallow events occur persistently throughout the year, with a seismicity rate of ∼3 events/day (Fig. 3b). We observe only one significant swarm-like period of > 20 events/day over almost 2 days in mid-July 2017 and two relatively smaller (∼16–18 events/day) one-day swarm like period in the end of September 2016 and May 2016 (Fig. 3b). The contribution of shallow events to the total seismic release is very small, with a cumulative moment release of 5.2×10^9 N-m (Fig. 3d), equivalent to one M_L 0.45 event. The biggest event was M_L 0.04 (Fig. 3a).

Since there are only four hydrophones and the shallow upper crustal velocity structure is not well known,

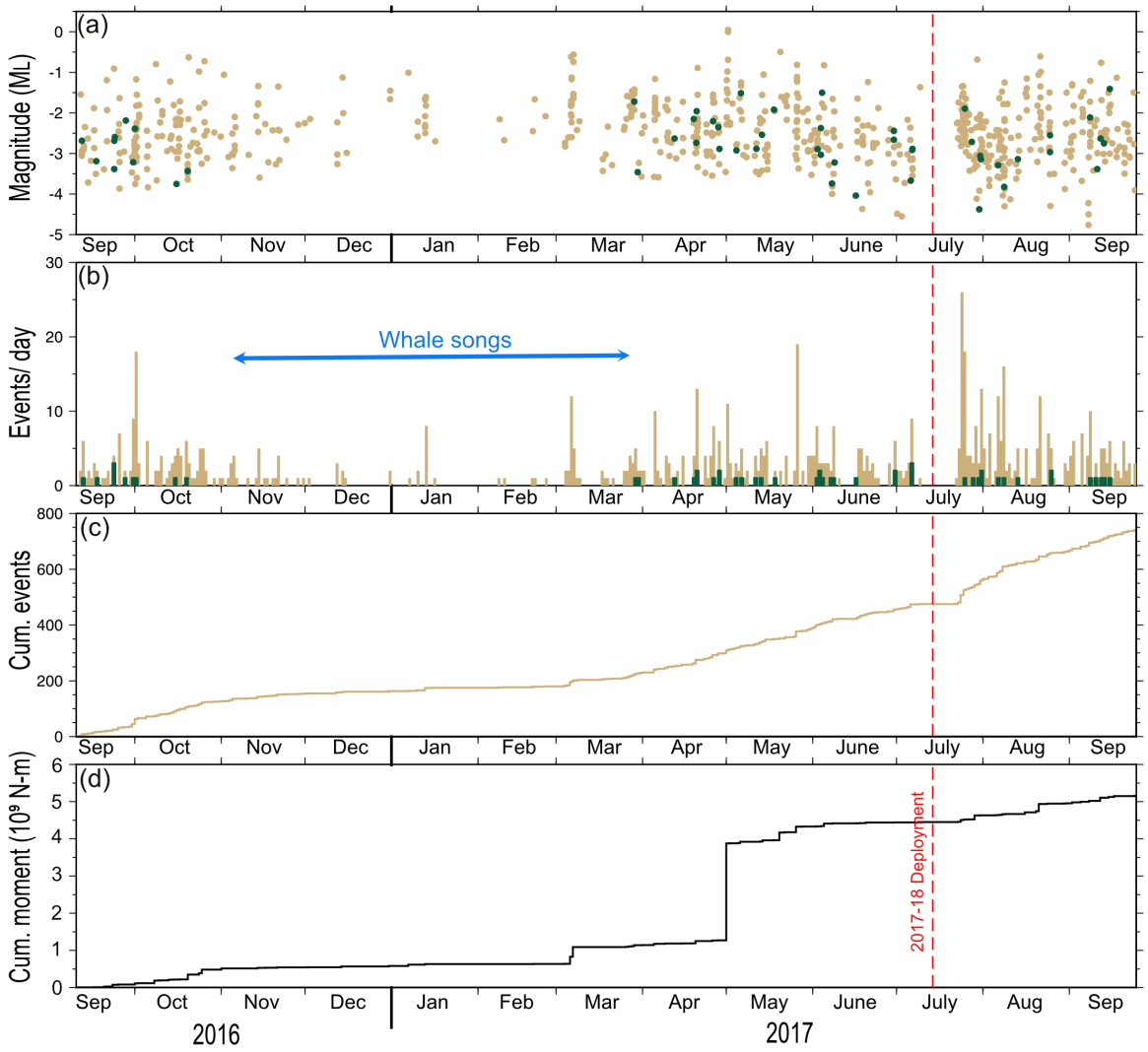

Figure 3 Temporal distribution of shallow microearthquakes (Type-1 events) located in the vicinity of Tour Eiffel hydrothermal vent site, Lucky Strike hydrothermal field. The red dashed line marks the 2017–2018 maintenance cruise and separates consecutive deployments. (a) Local magnitudes. Brown dots are events outside the Hydroctopus network; green dots are events inside the network. (b) Events/day. Blue arrow marks the approximate time period of abundant whale songs when shallow events were most difficult to detect (Fig. S9 in Supplementary material). Brown bars correspond to all shallow events, green bars correspond to events located inside the network. (c) Cumulative number of shallow events and (d) Cumulative seismic moment of shallow events.

event locations are not very well constrained. The mean RMS time error of all events is less than 10 ms, but the average event location uncertainties are ~232 m vertically and ~178 m horizontally (in the same range as the TAG shallow microearthquakes catalog; Fig. 4a and Fig. S10 in Supplementary Material; Pontbriand and Sohn, 2014). Most of the events are located outside the Hydroctopus network and seem to be randomly scattered horizontally (Fig. 4a). There is a small cluster a few hundred meters southeast of the Montségur hydrothermal site, including some of the larger events (M_L > -1.0) and the mid-July 2017 swarm events (Blue circles in Fig. 4a–b), and there is another small cluster in the vicinity of the Sintra and Y3 vent sites. Most events have depths < 300 m bsfr (below a seafloor reference depth defined at 1.7 km; (Fig. 4b). The scatter of the events appears to be real, as relocations done when swapping hydrophone positions are clustered in geometric forms related to the positions of the changed channels and give significantly higher mean RMS values (Fig. S11 and Text S3 in Supplementary Material).

Only 10% (76) of the shallow events and 4% of total cumulated seismic moment are located inside the network (Fig. 4a,c and Fig. S12a in Supplementary Material). All these events are very small (M_L < -1.5), and most are located within 200 m of the seafloor (Fig. 4b and Fig. S12b,c in Supplementary Material). We calculated the amplitude ratio between the center hydrophone (H3) and other hydrophones (H1, H2 & H4): for events classified as inside the network, the mean ratio is ~1.21 whereas for other events it is ~1.02, suggesting that events classified as inside-network are indeed closer to the central hydrophone.

3.3 Potential Source Mechanisms

The 740 near-seafloor microearthquakes have very short waveforms (~1 s), with only one clear direct P

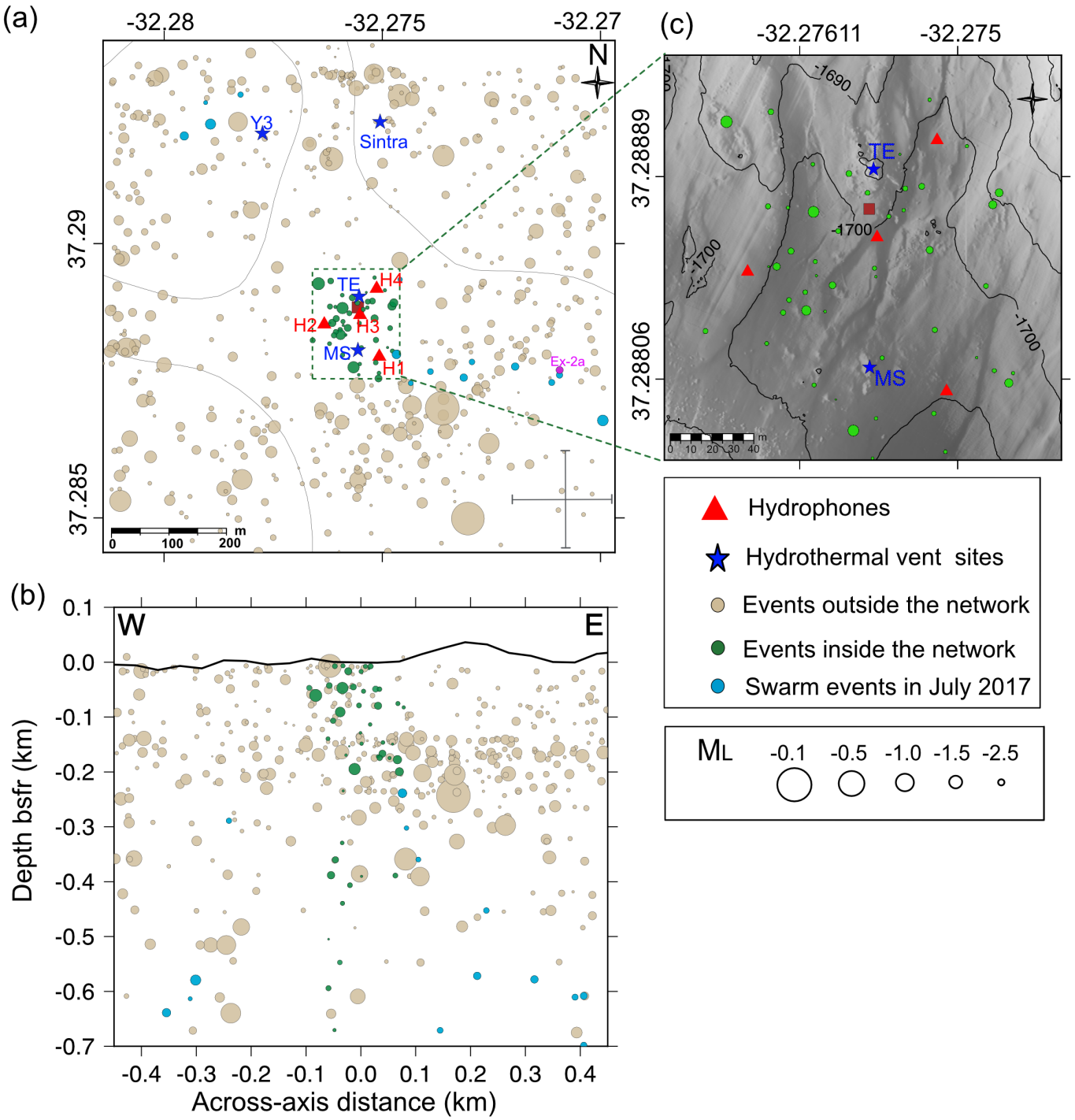

Figure 4 Spatial distribution of shallow microearthquakes (Type-1 events) in the vicinity of Tour Eiffel vent site. (a) Map view. Blue stars: Hydrothermal vent sites, Green dashed rectangle: The area of the Hydroctopus network, Brown dots: Events located outside the network, Green dots: Events located inside the network, Blue dots: Mid-July 2017 swarm events, Pink dot: Example event shown in Fig. 2a. The black cross at the bottom-right corner is the average horizontal uncertainty bars of all events. (b) Across-axis cross section through the center of the network. Depth is referenced beneath the seafloor reference (bsfr) depth at 1.7 km. (c) Zoomed view of the Hydroctopus network region. TE: Tour Eiffel, MS: Montségur

phase and with waveform patterns that change from sensor to sensor (Fig. 2a and Figs. S6–S7 in Supplementary Material). The extremely short event durations and the lack of S phase arrivals on the OBS vertical channel and PwP phase arrivals on Hydroctopus & OBS hydrophone channels suggest a non-double couple origin of these events (Pontbriand and Sohn, 2014).

Thermal contraction at the base of hydrothermal downflow zones is one non-double couple origin mechanism for microearthquakes recorded in the crust and a few hundred meters above axial magma lenses (Bohidar et al., 2024; Crawford et al., 2013; Sohn et al., 2004; Tolstoy et al., 2008). Cooling of magma intruded to a very shallow level in the crust could also create thermal contraction events at the very shallow depths of near-seafloor events, but there is no evidence for shallow magmatic injections below the Lucky Strike vents during the experiment as no earthquake swarms were

evident from the OBS data (Bohidar et al., 2024), nor was there any indication of seafloor eruption during yearly site submersible surveys.

Hydraulic fracturing and collapsing bubbles are non-double couple mechanisms proposed to generate shallow microearthquakes in hydrothermal systems (Dawson et al., 2012; Kedar et al., 1996, 1998; Miller et al., 1998). Hydraulic fracturing occurs when the fluid pressure exceeds the strength of the host rocks or the confining pressure and the fluid pressure of the hydrothermal system is less than or equal to the buoyancy pressure of the hydrothermal circulation (Cann and Strens, 1989). The buoyancy pressure at the bottom of Lucky Strike's primary hydrothermal system (2.5–3 km bsfr, Bohidar et al. (2024); Crawford et al. (2013)) is ∼ 10–15 MPa (Text S4 in Supplementary Material). The buoyancy pressure of shallower, secondary circulations will be even smaller, and significantly less than the 22 MPa confining pressure estimated at 200 m depth below seafloor in the Tour Eiffel area (Text S4 in Supplementary Material). It is therefore not possible to have shallow microearthquakes generated by hydraulic fracturing. The arguments developed by Pontbriand and Sohn (2014) against an origin of the TAG microearthquakes from vibrating or collapsing gas bubbles in the hydrothermal conduits also apply to the Tour Eiffel area: such bubbles would form in uprising end-member fluids and would thus not cause microearthquakes in areas of diffuse venting; they would also have to be unreasonably large to generate the observed seismic frequencies (Text S4 in Supplementary Material).

Reaction-driven cracking in response to anhydrite precipitation is the preferred mechanism by Pontbriand and Sohn (2014) for the generation of near-seafloor seismicity beneath the TAG hydrothermal site. Anhydrite is precipitated from entrained seawater heated to ∼150°C or more, either through conductive heating or by mixing with hot hydrothermal fluids (Bischoff and Seyfried, 1978). Anhydrite precipitation could fill the porosity, playing a key role in the permeability of the shallow substratum near hydrothermal vents (Guo et al., 2020; Lowell et al., 2003). Precipitation of anhydrite in veins and cracks leads to an increase in volume, which could cause fractures in the matrix and generate microearthquakes. Anhydrite precipitation is a plausible source mechanism for the shallow events reported in this study. Their scattered locations (Fig. 4a) could be due to the widespread distribution of diffuse venting in the Lucky Strike field (Barreyre et al., 2012). The depth limit of these microearthquakes would then correspond to the maximum depth of seawater entrainment depth in a broader hydrothermal upflow domain associated more with the diffuse venting than with the focused vent site.

The number of shallow events, and their magnitudes (∼3 events/day and local magnitude of completeness: -2.3; Fig. 3a,b), are much smaller than those observed beneath the TAG hydrothermal mound (∼243 events/day). TAG is a much larger hydrothermal site than Tour Eiffel (diameter ∼200 m; Humphris et al. (2015); Humphris and Kleinrock (1996); whereas TE is only ∼20 m in diameter), with a significantly higher estimated heat flux (∼1 GW for the TAG mound, Wichers (2005); and only ∼20 to 50 MW for TE, Mittelstaedt et al. (2012); Wheeler et al. (2024)). Heating of entrained seawater and anhydrite precipitation are therefore expected to be less prevalent at TE compared to TAG. This is in keeping with results from diffuse fluid chemistry at TE, that show little to no chemical evidence for anhydrite precipitation (Wheeler et al., 2024). Most of the shallow microearthquakes beneath the TAG mound are concentrated at a depth of ∼125 meters below seafloor (mbsf), which likely represents the maximum depth of seawater entrainment driven by the vigorous, focused venting at the main mound. In contrast, the scattered microearthquakes near TE occur at a depth range of 150–250 m, which would correspond to the maximum seawater entrainment within a broader hydrothermal upflow zone associated more with diffuse venting and they are not exclusively associated with the focused venting at TE.

If we further explore the anhydrite precipitation hypothesis, using the relation for a penny shaped fracture with only vertical strain (Pontbriand and Sohn, 2014), a minimum source volume of ∼0.007 m^3 is required to generate a M_L -2.48 earthquake (average M_L of shallow events catalog) for a stress drop equivalent or greater than the confining pressure (Text S4 in Supplementary Material). Assuming all 740 events were generated by anhydrite precipitation, the annual volume precipitated would be between 0.32 m^3 and 1.28 m^3 beneath the whole area of Fig. 4a (of which only 10% would be around the TE vent; Fig. 4c), compared to 27 m^3 to 513 m^3 below TAG (Pontbriand and Sohn, 2014).

4 Conclusion

1. We tested a new cost efficient, small aperture, temporally synchronized system recording four hydrophones on a single datalogger to precisely locate near-seafloor microearthquakes, which are potentially associated with shallow upflow of hot hydrothermal fluids and mineral precipitation in the secondary hydrothermal circulation domain near the Tour Eiffel hydrothermal vent site, Lucky Strike hydrothermal field.

2. We detected 740 near-seafloor microearthquakes between September 2016 and September 2017, with a seismicity rate of ∼3 events/day and local magnitudes ranging from -4 to -0.5. These events are characterized by short durations (∼1 s) and a lack of S and PwP (ocean surface reflected) phases.

3. Most of these events are located within ∼150–250 m below the seafloor and in a 900 m by 900 m area that extends beyond the Tour Eiffel site (diameter ∼20–30 m) and outside the ∼150 m aperture of the hydrophone network, with no clear spatial or temporal clustering.

4. These events may have originated through reaction-driven cracking in response to anhydrite precipitation from seawater entrained above a broad domain of mostly diffuse hydrothermal upflow. We interpret the much lower daily rates

of shallow seismicity beneath the Tour Eiffel site than those beneath the TAG hydrothermal mound, as evidence of much lower rates of anhydrite precipitation and less vigorous seawater entrainment due to lower hydrothermal heat fluxes.

5. The Hydroctopus system serves as a proof of concept for detecting shallow, near-seafloor microearthquakes associated with secondary hydrothermal circulation. In this study, the location uncertainties of these events is relatively high due to the limited number of hydrophones and the use of a poorly resolved upper crustal velocity model. In the future, deploying a denser network with higher sampling rates and/or incorporating improved velocity models could help better constrain event locations.

Data and code availability

Raw Hydroctopus datasets used in this study are available at Crawford et al. (2024); https://doi.org/10.17882/104520. Raw OBS datasets will be available at https://seismology.resif.fr/networks/#/4G. The software and codes used in this study include: SEISAN (Havskov and Ottemoller (1999); https://www.seisan.info/), ObsPy (Krischer et al. (2015); https://docs.obspy.org/), Pyrocko (Heimann et al. (2019); https://pyrocko.org/docs/current/index.html), multitaper (Prieto (2022); https://github.com/gaprieto/multitaper), NonLinLoc Version 7.0 (Lomax et al. (2000); http://alomax.free.fr/nlloc/), and GMT-6 (Wessel et al. (2019); https://www.generic-mapping-tools.org/).

Acknowledgements

We thank the captain and crew of the research vessels N/O *Atalante* for their help with the initial deployment of the Hydroctopus in 2016. We also thank all the contributors of the EMSO-Azores observatory for their help with the annual maintenance of the Hydroctopus in subsequent years. We thank Benjamin Wheeler for helpful discussion about the geochemical analysis. We also thank the editor, Zoe Krauss and one anonymous reviewer whose comments greatly helped improve our manuscript. SB was supported by the Université Paris Cité doctoral school funding and by ANR project Ridge Factory Slow (ANR-18-CE01-0002-01).

Competing interests

Authors declare no competing interests of any type regarding this work.

References

Arnulf, A., Harding, A., Singh, S., Kent, G., and Crawford, W. Nature of upper crust beneath the Lucky Strike volcano using elastic full waveform inversion of streamer data. *Geophysical Journal International*, 196(3):1471–1491, Dec. 2013. doi: 10.1093/gji/ggt461.

Baker, E. T., Massoth, G. J., Walker, S. L., and Embley, R. W. A method for quantitatively estimating diffuse and discrete hydrothermal discharge. *Earth and Planetary Science Letters*, 118 (1–4):235–249, July 1993. doi: 10.1016/0012-821x(93)90170-e.

Barreyre, T., Escartín, J., Garcia, R., Cannat, M., Mittelstaedt, E., and Prados, R. Structure, temporal evolution, and heat flux estimates from the Lucky Strike deep-sea hydrothermal field derived from seafloor image mosaics. *Geochemistry, Geophysics, Geosystems*, 13(4), Apr. 2012. doi: 10.1029/2011gc003990.

Barreyre, T., Escartin, J., Sohn, R., and Cannat, M. Permeability of the Lucky Strike deep-sea hydrothermal system: Constraints from the poroelastic response to ocean tidal loading. *Earth and Planetary Science Letters*, 408:146–154, Dec. 2014. doi: 10.1016/j.epsl.2014.09.049.

Bischoff, J. L. and Seyfried, W. E. Hydrothermal chemistry of seawater from 25 degrees to 350 degrees C. *American Journal of Science*, 278(6):838–860, June 1978. doi: 10.2475/ajs.278.6.838.

Bohidar, S., Crawford, W. C., and Cannat, M. Seismic Constraints on Hydrothermal Circulation and Magmato-Tectonic Interactions Beneath Lucky Strike Volcano, Mid-Atlantic Ridge. *Geochemistry, Geophysics, Geosystems*, 25(4), Apr. 2024. doi: 10.1029/2024gc011441.

Butterfield, D. A., Roe, K. K., Lilley, M. D., Huber, J. A., Baross, J. A., Embley, R. W., and Massoth, G. J. *Mixing, reaction and microbial activity in the sub-seafloor revealed by temporal and spatial variation in diffuse flow vents at axial volcano*, page 269–289. American Geophysical Union, 2004. doi: 10.1029/144gm17.

Cann, J. R. and Strens, M. R. Modeling periodic megaplume emission by black smoker systems. *Journal of Geophysical Research: Solid Earth*, 94(B9):12227–12237, Sept. 1989. doi: 10.1029/jb094ib09p12227.

Combier, V., Seher, T., Singh, S. C., Crawford, W. C., Cannat, M., Escartín, J., and Dusunur, D. Three-dimensional geometry of axial magma chamber roof and faults at Lucky Strike volcano on the Mid-Atlantic Ridge. *Journal of Geophysical Research: Solid Earth*, 120(8):5379–5400, Aug. 2015. doi: 10.1002/2015jb012365.

Cooper, M. J., Elderfield, H., and Schultz, A. Diffuse hydrothermal fluids from Lucky Strike hydrothermal vent field: Evidence for a shallow conductively heated system. *Journal of Geophysical Research: Solid Earth*, 105(B8):19369–19375, Aug. 2000. doi: 10.1029/2000jb900138.

Corliss, J. B., Dymond, J., Gordon, L. I., Edmond, J. M., von Herzen, R. P., Ballard, R. D., Green, K., Williams, D., Bainbridge, A., Crane, K., and van Andel, T. H. Submarine Thermal Springs on the Galápagos Rift. *Science*, 203(4385):1073–1083, Mar. 1979. doi: 10.1126/science.203.4385.1073.

Crawford, W., Cannat, M., Cobas, D., Besancon, S., Bohidar, S., and Daniel, R. HydrOCTOPUS : data from the EMSO-Azores observatory, 2016-2017, 2024. doi: 10.17882/104520.

Crawford, W. C., Rai, A., Singh, S. C., Cannat, M., Escartin, J., Wang, H., Daniel, R., and Combier, V. Hydrothermal seismicity beneath the summit of Lucky Strike volcano, Mid-Atlantic Ridge. *Earth and Planetary Science Letters*, 373:118–128, July 2013. doi: 10.1016/j.epsl.2013.04.028.

Cuvelier, D., Sarrazin, J., Colaço, A., Copley, J., Desbruyères, D., Glover, A. G., Tyler, P., and Serrão Santos, R. Distribution and spatial variation of hydrothermal faunal assemblages at Lucky Strike (Mid-Atlantic Ridge) revealed by high-resolution video image analysis. *Deep Sea Research Part I: Oceanographic Research Papers*, 56(11):2026–2040, Nov. 2009. doi: 10.1016/j.dsr.2009.06.006.

Dawson, P. B., Benítez, M. C., Lowenstern, J. B., and Chouet, B. A. Identifying bubble collapse in a hydrothermal system using hid-

den Markov models. *Geophysical Research Letters*, 39(1), Jan. 2012. doi: 10.1029/2011gl049901.

Edmond, J., Measures, C., Mangum, B., Grant, B., Sclater, F., Collier, R., Hudson, A., Gordon, L., and Corliss, J. On the formation of metal-rich deposits at ridge crests. *Earth and Planetary Science Letters*, 46(1):19–30, Dec. 1979. doi: 10.1016/0012-821x(79)90062-1.

Elderfield, H. and Schultz, A. Mid-Ocean Ridge Hydrothermal Fluxes and the Chemical Composition of the Ocean. *Annual Review of Earth and Planetary Sciences*, 24(1):191–224, May 1996. doi: 10.1146/annurev.earth.24.1.191.

Escartin, J., Barreyre, T., Cannat, M., Garcia, R., Gracias, N., Deschamps, A., Salocchi, A., Sarradin, P.-M., and Ballu, V. Hydrothermal activity along the slow-spreading Lucky Strike ridge segment (Mid-Atlantic Ridge): Distribution, heatflux, and geological controls. *Earth and Planetary Science Letters*, 431: 173–185, Dec. 2015. doi: 10.1016/j.epsl.2015.09.025.

Fouquet, Y., Ondréas, H., Charlou, J. L., Donval, J. P., Radford-Knoery, J., Costa, I., Lourenço, N., M. K., T., and Tivey, M. K. Atlantic lava lakes and hot vents. *Nature*, 377(6546):201–201, Sept. 1995. doi: 10.1038/377201a0.

Guo, Z., Rüpke, L. H., Fuchs, S., Iyer, K., Hannington, M. D., Chen, C., Tao, C., and Hasenclever, J. Anhydrite-Assisted Hydrothermal Metal Transport to the Ocean Floor—Insights From Thermo-Hydro-Chemical Modeling. *Journal of Geophysical Research: Solid Earth*, 125(7), June 2020. doi: 10.1029/2019jb019035.

Havskov, J. and Ottemoller, L. SeisAn Earthquake Analysis Software. *Seismological Research Letters*, 70(5):532–534, Sept. 1999. doi: 10.1785/gssrl.70.5.532.

Heimann, S., Vasyura-Bathke, H., Sudhaus, H., Isken, M. P., Kriegerowski, M., Steinberg, A., and Dahm, T. A Python framework for efficient use of pre-computed Green's functions in seismological and other physical forward and inverse source problems. *Solid Earth*, 10(6):1921–1935, Nov. 2019. doi: 10.5194/se-10-1921-2019.

Humphris, S., Herzig, P., and Miller, D. Proceedings of the Ocean Drilling Program, Initial Reports, Volume 158. TAG: Drilling an Active Hydrothermal System on a Sediment-free Slow Spreading Ridge: Covering Leg 158 of the Cruise of the Drilling Vessel" JOIDES Resolution", Las Palmas, Gran Canaria, to Las Palmas, Gran Canaria, Site 957, 23 September-22 November 1994. *Texas A & M University Ocean Drilling Program*, 158, 1995.

Humphris, S. E. and Kleinrock, M. C. Detailed morphology of the TAG Active Hydrothermal Mound: Insights into its formation and growth. *Geophysical Research Letters*, 23(23):3443–3446, Nov. 1996. doi: 10.1029/96gl03079.

Humphris, S. E., Fornari, D. J., Scheirer, D. S., German, C. R., and Parson, L. M. Geotectonic setting of hydrothermal activity on the summit of Lucky Strike Seamount (37°17′N, Mid-Atlantic Ridge). *Geochemistry, Geophysics, Geosystems*, 3(8):1–25, Aug. 2002. doi: 10.1029/2001gc000284.

Humphris, S. E., Tivey, M. K., and Tivey, M. A. The Trans-Atlantic Geotraverse hydrothermal field: A hydrothermal system on an active detachment fault. *Deep Sea Research Part II: Topical Studies in Oceanography*, 121:8–16, Nov. 2015. doi: 10.1016/j.dsr2.2015.02.015.

Juniper, S. K., Martineu, P., Sarrazin, J., and Gélinas, Y. Microbial-mineral floc associated with nascent hydrothermal activity on CoAxial Segment, Juan de Fuca Ridge. *Geophysical Research Letters*, 22(2):179–182, Jan. 1995. doi: 10.1029/94gl02436.

Kedar, S., Sturtevant, B., and Kanamori, H. The origin of harmonic tremor at Old Faithful geyser. *Nature*, 379(6567):708–711, Feb. 1996. doi: 10.1038/379708a0.

Kedar, S., Kanamori, H., and Sturtevant, B. Bubble collapse as the source of tremor at Old Faithful Geyser. *Journal of Geophysical Research: Solid Earth*, 103(B10):24283–24299, Oct. 1998. doi: 10.1029/98jb01824.

Krischer, L., Megies, T., Barsch, R., Beyreuther, M., Lecocq, T., Caudron, C., and Wassermann, J. ObsPy: a bridge for seismology into the scientific Python ecosystem. *Computational Science & Discovery*, 8(1):014003, May 2015. doi: 10.1088/1749-4699/8/1/014003.

Langmuir, C., Humphris, S., Fornari, D., Van Dover, C., Von Damm, K., Tivey, M., Colodner, D., Charlou, J.-L., Desonie, D., Wilson, C., Fouquet, Y., Klinkhammer, G., and Bougault, H. Hydrothermal vents near a mantle hot spot: the Lucky Strike vent field at 37°N on the Mid-Atlantic Ridge. *Earth and Planetary Science Letters*, 148(1–2):69–91, Apr. 1997. doi: 10.1016/s0012-821x(97)00027-7.

Lister, C. R. B. On the Thermal Balance of a Mid-Ocean Ridge. *Geophysical Journal International*, 26(5):515–535, Apr. 1972. doi: 10.1111/j.1365-246x.1972.tb05766.x.

Lister, C. R. B. On the Penetration of Water into Hot Rock. *Geophysical Journal International*, 39(3):465–509, Dec. 1974. doi: 10.1111/j.1365-246x.1974.tb05468.x.

Lomax, A., Virieux, J., Volant, P., and Berge-Thierry, C. *Probabilistic Earthquake Location in 3D and Layered Models*, page 101–134. Springer Netherlands, 2000. doi: 10.1007/978-94-015-9536-0_5.

Lowell, R. P. and Yao, Y. Anhydrite precipitation and the extent of hydrothermal recharge zones at ocean ridge crests. *Journal of Geophysical Research: Solid Earth*, 107(B9), Sept. 2002. doi: 10.1029/2001jb001289.

Lowell, R. P., Rona, P. A., and Von Herzen, R. P. Seafloor hydrothermal systems. *Journal of Geophysical Research: Solid Earth*, 100 (B1):327–352, Jan. 1995. doi: 10.1029/94jb02222.

Lowell, R. P., Yao, Y., and Germanovich, L. N. Anhydrite precipitation and the relationship between focused and diffuse flow in seafloor hydrothermal systems. *Journal of Geophysical Research: Solid Earth*, 108(B9), Sept. 2003. doi: 10.1029/2002jb002371.

Miller, A. D., Foulger, G. R., and Julian, B. R. Non-double-couple earthquakes 2. Observations. *Reviews of Geophysics*, 36(4): 551–568, Nov. 1998. doi: 10.1029/98rg00717.

Mittelstaedt, E., Escartín, J., Gracias, N., Olive, J., Barreyre, T., Davaille, A., Cannat, M., and Garcia, R. Quantifying diffuse and discrete venting at the Tour Eiffel vent site, Lucky Strike hydrothermal field. *Geochemistry, Geophysics, Geosystems*, 13(4), Apr. 2012. doi: 10.1029/2011gc003991.

Ondréas, H., Cannat, M., Fouquet, Y., Normand, A., Sarradin, P. M., and Sarrazin, J. Recent volcanic events and the distribution of hydrothermal venting at the Lucky Strike hydrothermal field, Mid-Atlantic Ridge. *Geochemistry, Geophysics, Geosystems*, 10 (2), Feb. 2009. doi: 10.1029/2008gc002171.

Pontbriand, C. W. and Sohn, R. A. Microearthquake evidence for reaction-driven cracking within the Trans-Atlantic Geotraverse active hydrothermal deposit: Microearthquakes at TAG active mound. *Journal of Geophysical Research: Solid Earth*, 119(2): 822–839, Feb. 2014. doi: 10.1002/2013jb010110.

Prieto, G. A. The Multitaper Spectrum Analysis Package in Python. *Seismological Research Letters*, 93(3):1922–1929, Mar. 2022. doi: 10.1785/0220210332.

Ramondenc, P., Germanovich, L. N., Von Damm, K. L., and Lowell, R. P. The first measurements of hydrothermal heat output at 9°50′N, East Pacific Rise. *Earth and Planetary Science Letters*, 245(3–4):487–497, May 2006. doi: 10.1016/j.epsl.2006.03.023.

Singh, S. C., Crawford, W. C., Carton, H., Seher, T., Combier, V., Cannat, M., Pablo Canales, J., Düsünür, D., Escartin, J., and

Miguel Miranda, J. Discovery of a magma chamber and faults beneath a Mid-Atlantic Ridge hydrothermal field. *Nature*, 442 (7106):1029–1032, Aug. 2006. doi: 10.1038/nature05105.

Sohn, R. A., Barclay, A. H., and Webb, S. C. Microearthquake patterns following the 1998 eruption of Axial Volcano, Juan de Fuca Ridge: Mechanical relaxation and thermal strain. *Journal of Geophysical Research: Solid Earth*, 109(B1), Jan. 2004. doi: 10.1029/2003jb002499.

Tolstoy, M., Waldhauser, F., Bohnenstiehl, D. R., Weekly, R. T., and Kim, W.-Y. Seismic identification of along-axis hydrothermal flow on the East Pacific Rise. *Nature*, 451(7175):181–184, Jan. 2008. doi: 10.1038/nature06424.

Wessel, P., Luis, J. F., Uieda, L., Scharroo, R., Wobbe, F., Smith, W. H. F., and Tian, D. The Generic Mapping Tools Version 6. *Geochemistry, Geophysics, Geosystems*, 20(11):5556–5564, Nov. 2019. doi: 10.1029/2019gc008515.

Wheeler, B., Cannat, M., Chavagnac, V., and Fontaine, F. Diffuse Venting and Near Seafloor Hydrothermal Circulation at the Lucky Strike Vent Field, Mid-Atlantic Ridge. *Geochemistry, Geophysics, Geosystems*, 25(3), Feb. 2024. doi: 10.1029/2023gc011099.

Wichers, S. *Verification of numerical models for hydrothermal plume water through field measurements at TAG*. Massachusetts Institute of Technology and Woods Hole Oceanographic Institution, 2005. doi: 10.1575/1912/1640.

Wilcock, W. S. and Delaney, J. R. Mid-ocean ridge sulfide deposits: Evidence for heat extraction from magma chambers or cracking fronts? *Earth and Planetary Science Letters*, 145(1–4):49–64, Dec. 1996. doi: 10.1016/s0012-821x(96)00195-1.